Increasing Heat Transfer in Microchannels with Surface Acoustic Waves

S. Berry[1]
[1]MIT Lincoln Laboratory, Lexington, MA, USA
[1]Corresponding author: sberry@LL.mit.edu

Abstract: In this numerical study, surface acoustic waves (SAWs) are evaluated as a potential disruptive flow technology for enhancing heat transfer in microchannels. Using COMSOL, the physics governing acoustics, single-phase-fluid flow and heat transfer are coupled. First, the harmonic time behavior of the acoustic motion of the fluid resulting from the surface acoustic wave (SAW) is solved. Next, using results from the acoustic solution, source terms are added to the continuity and momentum equations. The results show that acoustic streaming can disrupt the bulk fluid flow, creating rotating vortices within the microchannel and enhancing heat transfer. Under the right flow conditions, the resulting circulating flow disrupts the thermal boundary layer, increasing heat flux across the microchannel. As the flow rate increases in the microchannel, advection dominates the flow, overwhelming the ability for vortices to be generated by acoustic streaming. The results show that when the bulk microchannel stream velocity is less than the acoustic streaming velocity, there is an enhancement in heat transfer from SAW.

Keywords: Acoustic streaming, surface acoustic waves, thermal management, microfluidics, heat transfer

1. Introduction

As the trend in electronics continues towards higher integration density and higher power devices, current remote cooling technology will not be able to handle the predicted levels of heat removal necessary. A new paradigm for embedded cooling is required [1]. Microfluidic cooling holds potential promise for these thermal management challenges. To date, there has been a large amount of research and technology development in microfluidic cooling, both in single-phase and two-phase flow [2-4]. However, a potential limitation, especially for single-phase flow for thermal management of microelectronics, is the high flow rates and the high pressures often required to generate the desired increases in convective heat transfer in microchannels. The limiting factor in convective heat transfer is that a thermal boundary layer forms at the fluid/wall interface. The heat flux across this layer is limited to the conduction of the fluid. Therefore, effective methods for disrupting the thermal boundary layer may help to reduce the pumping requirements for microfluidic cooling.

In this paper SAWs are evaluated as a disruptive flow technology for increasing heat transfer in microchannels. SAWs are ultrasonic waves that propagate along an elastic surface. When these waves come in contact with a fluid medium, they can couple with the fluid, driving fluid flow. This effect is known as acoustic streaming [5]. Details describing this phenomenon can be found in [5-7] and the references within. Several applications of SAWs in microfluidics include mixing [8] and acoustophoresis for particle and cell sorting [9, 10].

To evaluate the effectiveness of acoustic streaming on heat transfer in microchannel flows, 2D numerical simulations were performed. SAWs were coupled with single-phase, laminar flow in order to drive circulating and chaotic flow in a microchannel. The average heat flux across the microchannel was determined for various SAWs, flow rates, and channel parameters.

2. Use of COMSOL Multiphysics

To simulate the acoustic streaming and the effects on heat transfer, COMSOL Multiphysics 4.3b was implemented. The modeling approach used in this study was similar to the approach used in [11].

The numerical simulation challenge is that SAWs operate in the MHz range and behave with harmonic time dependence, but viscous effects in the fluid happen on a time scale of

msec or slower, requiring a time-averaged response of the acoustic oscillations. To model the SAW/viscous flow interaction, perturbation theory is one approach often used [6]. The theory behind this method can be found in [6, 8, 11]. In this approach, acoustic motion to the first-order is solved and then using first-order results, second-order values are solved in the conservation equations for fluid flow and heat transfer.

2.1 First-order equations

To more accurately capture the acoustic behavior, the full thermoviscous first-order equations were solved using the Thermoacoustics Physics interface in COMSOL. To the first-order, the acoustic field from SAW can be described by the thermodynamic heat transfer equation for temperature T_1 eqn. (1a), the kinematic continuity equation in terms of pressure p_1 eqn. (1b), and the momentum equation for the velocity field u_1 eqn. (1c), respectively,

$$\frac{\partial T_1}{\partial t} = D\nabla^2 T_1 + \frac{\alpha T_0}{\rho_o C_p}\frac{\partial p_1}{\partial t}, \qquad (1a)$$

$$\frac{\partial p_1}{\partial t} = \frac{1}{\gamma\kappa}\left[\alpha\frac{\partial T_1}{\partial t} - \nabla\cdot u_1\right], \qquad (1b)$$

$$\rho_o\frac{\partial u_1}{\partial t} = -\nabla p_1 + \mu\nabla^2 u_1 + \left(\mu_B + \frac{\mu}{3}\right)\nabla(\nabla\cdot u_1), \qquad (1c)$$

where D is the thermal diffusivity, T_O is the wall temperature, ρ_o is the mass density, α is the thermal expansion coefficient, γ is the specific heat capacity ratio, κ is the isentropic compressibility and μ_B and μ are the bulk and shear dynamic viscosities respectively. It is assumed that all the first-order fields have a harmonic time dependence $e^{-i\omega t}$ resulting from the ultrasound field. This reduces the derivatives in eqn. (1) to factors of $-i\omega$. A full derivation of these equations, assuming harmonic time dependence, can be found in [11].

The non-linear interaction of the first-order fields in the fluid occurs in a thin thermoviscous boundary near the surface. One of the numerical challenges is resolving the thermoviscous boundary layers. The thermal and viscous boundary layers, δ_{th} and δ, respectively, in a fluid resulting from an ultrasound wave can be estimated from,

$$\delta_{th} = \sqrt{\frac{2D}{\omega}}, \text{ and } \delta = \sqrt{\frac{2\mu}{\omega}}. \qquad (2)$$

The values of these boundary layers are typically 1000 times smaller than the microchannel dimensions. This requires a very fine mesh near all boundaries, adding to the computation cost. Viscous interactions with this boundary layer drive the acoustic streaming in the bulk fluid.

2.2 Second-order equations

Coupling between the first-order equations and second-order equations will be done through the velocity, u_2 and pressure, p_2. Since thermal effects in the first-order are small [11], no coupling of the temperature field T_2 and first-order equations are done. Because viscous effects happen on a larger time-scale than the ultrasound time-scale, the dependent variables need to be time-averaged over a period of excitation. The second-order, time-averaged continuity equation eqn. (3a), momentum equation eqn. (3b) and energy equation eqn. (3c) are,

$$\rho_o\nabla\langle u_2\rangle = -\nabla\cdot\langle\rho_1 u_1\rangle, \qquad (3a)$$

$$\mu\nabla^2\langle u_2\rangle + \left(\mu_B + \frac{\mu}{3}\right)\nabla\nabla\cdot\langle u_2\rangle - \nabla\langle p_2\rangle = \langle\rho_1\frac{\partial u_1}{\partial t}\rangle + \rho_o\langle(u_1\cdot\nabla)u_1\rangle, \qquad (3b)$$

$$\rho_o C_p\langle u_2\rangle\nabla T_2 = \nabla\cdot(K\nabla T_2) + Q, \qquad (3c)$$

where <x> denotes the time average quantity x over a full oscillation time period. As can be seen, the products of the first-order results act as source terms (right-hand side of eqn. (3a) and (3b)) for the second-order equations. These equations were solved using the Conjugate Heat Transfer interface for laminar flow, modified to include the first-order source terms.

2.3 Source terms

The source terms associated with momentum equation (right-hand side of eqn. (3b)) are

directly implemented in COMSOL as a volume force. The source term for the continuity equation (right-hand side of eqn. (3a)) requires the constitutive equation in COMSOL to be altered. This is done by defining a "weak contribution" that is applied to the element test function.

The source terms from the first-order results are complex-valued fields of the form *A(t)* and *B(t)* with harmonic time dependence $e^{-i\omega t}$. The time average for complex-value fields is given by the real-part rule:

$\langle A(t)B(t)\rangle = \frac{1}{2}Re[A(0)^{*}B(0)]$, where *A(0)** represents the complex conjugation.

3. Numerical Model

Figure 1 shows the channel geometry and boundary conditions used in the 2D simulations. The simulations were divided into two steps. In Step 1, the first-order equations were solved using the Thermoacoustics Physics interface and the boundary conditions shown in Fig. 1a. In Step 2, the time-averaged second-order flow $\langle u_2 \rangle$ and temperature in the channel was determined using the Conjugate Heat Transfer interface for steady-state laminar flow. The boundary conditions associated with Step 2 are shown in Fig. 1b.

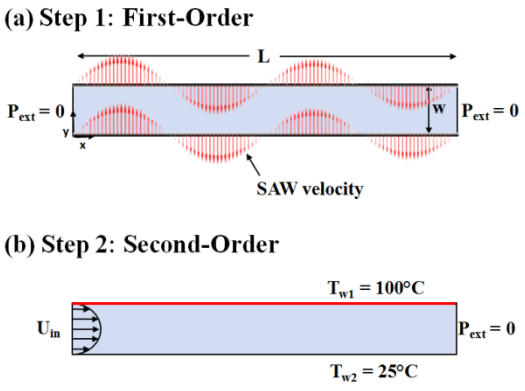

Figure 1. Boundary conditions used in the simulations for a water filled microchannel. (a) Boundary conditions for Step 1: First-order thermoacoustics simulation. SAW introduced as a velocity on the top and bottom of channel walls (exaggerated scale). (b) Boundary conditions for Step 2: Second-order conjugate heat transfer simulation. Fixed temperatures applied to top and bottom channel walls, and laminar inlet velocity U_{in} applied to one end of the channel.

In Step 1, the SAW is introduced as a velocity in the form of $i\omega d_o$ on the channel walls, where d_o is the SAW amplitude, which is typically small, of the order of 0.1 nm [9], and ω is the SAW frequency in radians/s. The standing wave from SAW is applied along both the top and bottom of the microchannel in order to maximize the bulk streaming velocity. The velocity is applied normal to the walls and is defined as,

$$u_{bc}(x,L) = \omega d_o e^{-\alpha x}\sin\left(n\pi\frac{x}{L}\right), \qquad (4)$$

where α is an attenuation coefficient defined as [9],

$$\alpha = \frac{\rho_f c_f}{\rho_s c_s \lambda_s}, \qquad (5)$$

where ρ_f and ρ_s are the fluid and solid densities respectively, c_f and c_s are the speed of sound in the fluid and solid respectively, and λ_s is the SAW wavelength in the solid. n is the number of waves along the length of the channel given by: L/λ_s. The pressure acting on the left and right channel wall was set to p_{ext} = 0 Pa, representing an open channel.

In Step 2 the first-order fields (u_1 and p_1) were included as source terms in the equations (3a) and (3b). A laminar flow inlet boundary condition was applied to the left channel face for different average velocities, U_{in}, and a pressure boundary of p_{ext} = 0 Pa was applied to the right face. A constant wall temperature of T_{w1} = 100°C was applied to the top channel wall and a constant wall temperature of T_{w2} = 25°C was applied to the bottom channel wall.

The same computational mesh was used in both steps. The maximum triangular element size in the bulk domain was set at 7.5δ. Through the viscous boundary layer thickness, a minimum of eight boundary elements were used. Key model parameters used to determine length scales are listed in Table 1. In the simulations, temperature dependent material properties for water were used.

Table 1: Model parameters

Water @25°C			
Density	ρ_f	998	kg/m^3
Speed of sound	c_f	1495	m/s
Dynamic viscosity	μ	8.90e-4	Ps s
Thermal diffusivity	D	1.43e-7	m^2/s
Solid*			
Density	ρ_s	4650	kg/m^3
Speed of sound	c_s	3990	m/s

*single crystal Lithium Niobate

4.0 Results

The initial simulations performed in this study did not include solving the energy equation. Only the continuity and momentum equations for laminar flow were used in the second-order simulation. These simulations were used to validate the modeling procedure and understand the effects of SAW and microchannel geometry parameters.

Figure 2 shows contour plots for the first-order fields, p_1, T_1, u_{1x}, and u_{1y}, for the velocity boundary condition shown in Fig. 1a. The input values were: f = 15 MHz, d_o = 0.1 nm, L = 1000 µm, and w = 50 µm. At this frequency, 4 standing waves act over the length of the channel.

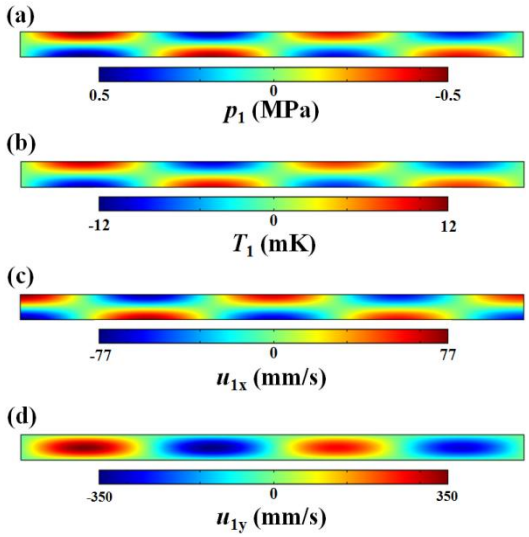

Figure 2. Contour plots of the first-order fields for a water filled channel (L = 1000 µm, w = 50 µm) excited by a velocity boundary condition applied to the top and bottom channel wall. SAW frequency, f = 15 MHz, and amplitude, d_o = 0.1 nm. (a) pressure p_1, (b) temperature T_1, (c) horizontal velocity u_{1x}, and (d) vertical velocity u_{1y}.

As can be seen, the temperature increase from the SAW is small, on the order of mK. This supports the argument not to couple the temperature field to the second-order equations. The amplitudes of p_1 and T_1 have the same spatial structure. The spatial structure of u_{1x} is the same as p_1 only shifted by $\lambda/4$. The spatial structure of u_{1y} has a half-wave resonance with 15 MHz (based on wavelength through the fluid media). The channel width was chosen to be $\lambda/2$ in order to achieve this effect. As will be discussed, having a half-wave resonance increases the strength of the second-order acoustic streaming velocity.

Using the first-order results presented in Figure 2, the time-averaged second-order fields for different inlet velocities were found. Figure 3 shows the resulting steady-state velocity field in the microchannel without any inlet flow.

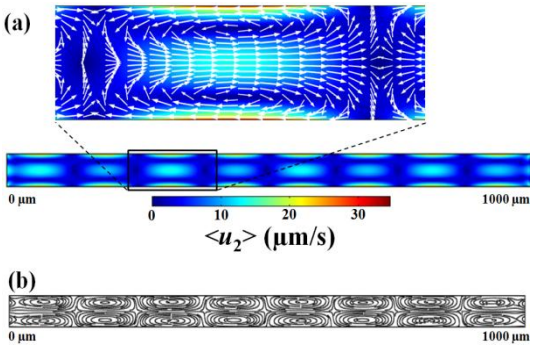

Figure 3. Time-averaged second-order velocity field for a water filled channel (L = 1000 µm, w = 50 µm) with no inlet flow, excited by first-order fields shown in Figure 2. SAW frequency, f = 15 MHz, and amplitude, d_o = 0.1 nm. (a) Contour plot of velocity magnitude <u_2>. Zoomed-in insert overlays a vector plot of velocity <u_2>. (b) Streamlines from resulting velocity field clearly show multiple Rayleigh streaming vortices.

The time-averaged velocity field in Figure 3 contains multiple Rayleigh streaming vortices along the channel length. Across the width there are two, symmetric Rayleigh streaming vortices, as evidenced by the streamlines in Fig. 3b. Not shown are the boundary streaming vortices

(Schlicting vortices [11]) that are generated in the viscous boundary layer close to the channel walls. For this simulation condition the viscous boundary is $\delta = 138$ nm. It is important to note, the boundary streaming vortices are driven by the non-linear interaction of the first-order fields, and the Rayleigh streaming vortices arise from viscous interactions with the boundary vortices [11]. The streaming velocity is a maximum close to the top and bottom wall just outside the viscous boundary layer and its magnitude is an order of magnitude lower than the first-order acoustic velocity.

The effect of inlet velocity on the time-average velocity field is shown in Figure 4 as streamlines. Results are for three different inlet velocities, U_{in} = 1 µm/s, 10 µm/s, and 100 µm/s.

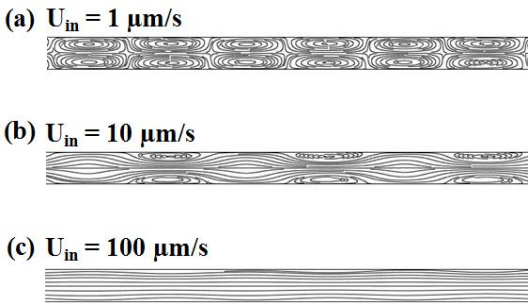

Figure 4. Streamlines resulting from the time-averaged second-order velocity field for a water filled channel (L = 1000 µm, w = 50 µm) for different inlet velocities, excited by first-order fields shown in Figure 2. SAW frequency, f = 15 MHz, and amplitude, d_o = 0.1 nm. (a) U_{in} = 1 µm/s. (b) U_{in} = 10 µm/s. (c) U_{in} = 100 µm/s.

As the inlet velocity increases, the effect of acoustic streaming in the bulk fluid becomes reduced, as is evident from the reduction in Rayleigh streaming vortices. For inlet velocities less than or equal to the maximum streaming velocity, Rayleigh streaming vortices can form in the channel. When the inlet velocity is greater than the streaming velocity, advection dominates the channel flow. In order to have SAWs be useful at enhancing heat transfer and disrupting the thermal boundary layer in a microchannel, the bulk channel flow must be less than or equal to the maximum streaming velocity.

For the results presented in Figure 4, the Reynolds number ($Re = \frac{\rho_f U_{in} w}{\mu}$) based on the inlet velocities are all Re <<1. This is a very low flow and would not be effective at convecting heat along the channel. This means the streaming velocity has to increase in order to permit higher inlet flows and provide more meaningful heat removal potential.

It was observed that the maximum streaming velocity occurs when the channel width was set to $\lambda/2$, where λ is the wavelength of ultrasound wave in the fluid. When there is no half-wave resonance, the acoustic coupling to the fluid is weak. In addition to setting the channel width to $\lambda/2$, the streaming velocity is strongly dependent on SAW amplitude. Figure 5 plots the maximum streaming velocity vs. SAW amplitude for different frequencies. The SAW amplitudes ranged from 0.1 nm to 10 nm. The results show that the streaming velocity is quadratic in SAW amplitude for all frequencies.

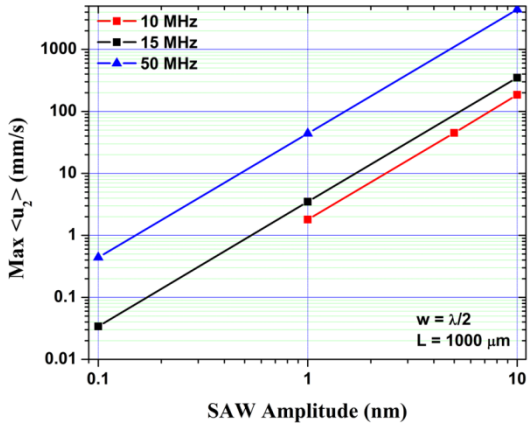

Figure 5. Maximum streaming velocity vs. SAW amplitude, d_o. The channel geometry was L = 1000 µm and $w = \lambda/2$, where λ is the wavelength in the fluid.

To evaluate the effectiveness of using SAWs to enhance heat transfer in microchannels, it will be assumed that through the proper design of the SAW resonator, large displacement amplitudes >1 nm in the piezoelectric material can be achieved. Recent modeling work suggests high mechanical displacement in the piezoelectric material is feasible [12].

All the heat transfer simulations were carried out for channel geometries having $w = \lambda/2$, and SAW amplitudes d_o = 10 nm, which is a ~100 times greater than typical displacements. A SAW frequency of f = 7.5 MHz was used, which conveniently sets the channel width to 100 µm.

Figure 6 shows the steady-state results from the conjugate heat transfer simulations for a water filled channel (L = 1000 µm, w = 100 µm) and Re = 1. Fig. 6a shows the streamlines and temperature contours for the case when there is no SAW, only laminar flow. In this case, parallel streamlines are formed and the temperature contour plot clearly shows the thermal boundary layer growth along the channel. Note, an entry length equal to the channel width was added to the model in order to easily observe the thermal boundary layer and avoid artificial inlet effects. Fig. 6b shows the time-averaged second-order velocity (streamlines) and temperature contours for case when SAW is included. For this flow (Re = 1), the Rayleigh streaming vortices can form. The average velocity magnitude of these vortices is ~ 70 mm/s. The spatial structures of the vortices have non-symmetrical shapes which is a result of using temperature dependent material properties for the water. These streaming vortices disrupt the thermal boundary layer as can be seen in the temperature contour plot.

To compare the two results, the total heat flux q, along the heated wall was determined. For the no-SAW case, q = 54 W/cm^2. With the SAW included, q = 171 W/cm^2. This was greater than a factor of 3x increase.

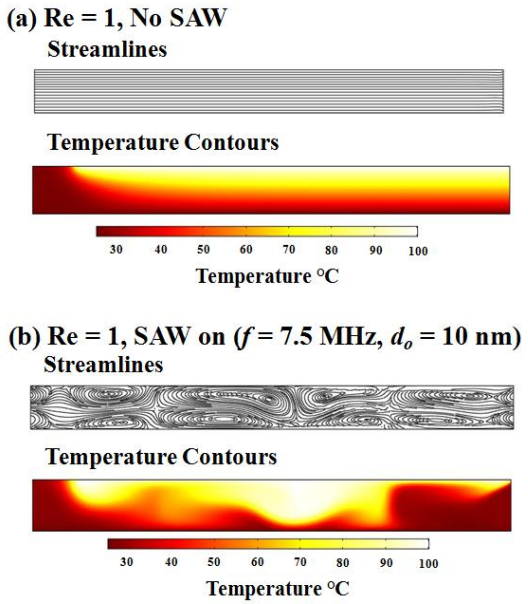

Figure 6. Results from conjugate heat transfer simulations for a water filled channel (L = 1000 µm, w = 100 µm) with the boundary condition shown in Fig. 1b. (a) Results for no SAW, only laminar inlet flow of Re = 1. (b) Results for SAW coupled with laminar inlet flow of Re = 1. The first-order fields were excited by velocity boundary condition applied to the top and bottom channel walls for SAW frequency, f = 7.5 MHz, and amplitude, d_o = 10 nm.

Figure 7 plots the average heat flux on the heated wall vs. Re number for different SAW amplitudes. The results show, that for the right flow conditions there is an increase in heat transfer due to SAW. However, as the Re number increases the effect of the SAW on heat transfer is reduced since no streaming vortices can form to disrupt the thermal boundary layer.

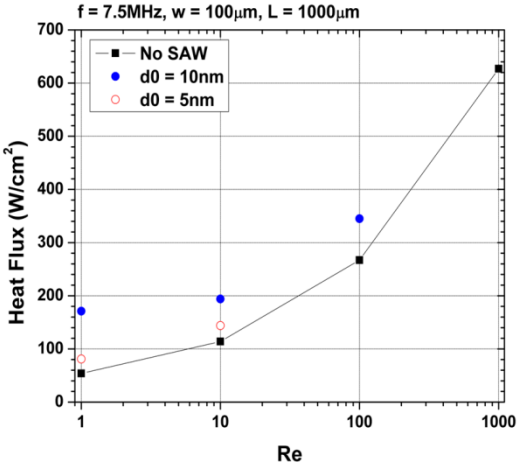

Figure 7. Total heat flux along heated wall vs. Re for a water filled channel (L = 1000 µm, w = 100 µm). Solid line represents no SAW, only inlet flow. Data points represent coupled SAW and inlet flow for different SAW amplitudes. First-order fields generated for a SAW frequency, f = 7.5 MHz.

5. Conclusions

In this numerical study, surface acoustic waves were evaluated as a potential disruptive flow technology for enhancing heat transfer in microchannels. A COMSOL modeling procedure was developed that captures the acoustic behavior in a water filled channel by first solving thermoviscous first-order equations, and then solving the time-averaged, second-order equations, including the energy equation for fluid flow and temperature. It was observed that under the right conditions, the acoustic streaming, when coupled to low-laminar flow can disrupt the thermal boundary layer and

increase the heat flux in the channel compared to only laminar flow. The results show that when the bulk channel stream velocity is less than the acoustic streaming velocity, rotating vortices can form, disrupting the flow. When the bulk channel stream velocity is greater than the acoustic streaming velocity, advection dominates the flow, and no rotating vortices can form.

6. Acknowledgements

This work was sponsored by the Department of the Air Force under Air Force Contract #FA8721-05-C-0002. Opinions, interpretations, conclusions and recommendations are those of the author are not necessarily endorsed the United Stated Government. In addition, thank you to Dr. Mads Jakob Herring Jensen of COMSOL for guidance and assistance in developing the numerical model.

7. References

[1] A. Bar-Cohen and K. Geisler, "Cooling the Electronic Brain," *Mechanical Engineering*, **133**, 38-41 (2011).

[2] S. Kandlikar, and W. Grande, "Evaluation of Single Phase Flow in Microchannels for High Heat Flux Chip Cooling – Thermohydraulic Perfomance Enhancement and Fabrication Technology," *Heat Transfer Engineering*, **25**, 5-16 (2004).

[3] B. Dang, M. Bakir, D. C. Sekar, C. King, Jr., and J. Meindl, "Integrated Microfluidic Cooling and Interconnects for 2D and 3D Chips," *IEEE Transactions on Advanced Packaging*, **33**, 79-87 (2010).

[4] A. Bar-Cohen, J. Sheehan, and E. Rahim, "Two-Phase Thermal Transport in Microgap Channels – Theory, Experimental Results and Predictive Relations," *Microgravity Sci. Technol.*, **24**, 1-15 (2012).

[5] N. Riley, "Acoustic Streaming," *Theoret. Comput. Fluid Dynamics*, **10**, 349-356 (1998).

[6] X. Ding, P. Li, S. C. S. Lin, Z. S. Stratton, N. Nama, F. Guo, D. Slotcavage, X. Mao, J. Shi, F. Costanzo, and T. J. Huang, "Surface acoustic wave microfluidics," *Lab on a Chip*, **13**, 3626-3649 (2013).

[7] S. Sankaranaryanan, S. Culer, V. R. Bhethanabotla, and B. Joseph, "Flow induced by acoustic streaming on surface-acoustic-wave devices and its application in biofouling removal: A computational study and comparisons to experiment," *Physical Review E*, **77**, 066308 (2008).

[8] M. K. Tan, L. Y. Yeo, and J. R. Friend, Rapid fluid flow and mixing induced in microchannels using surface acoustic waves," *EPL*, **87**, 47003 (2009).

[9] M. Gedge, and M. Hill, "Acoustofluidics 17: Theory and applications of surface acoustic wave devices for particle manipulation," *Lab on a Chip*, **12**, 2998-3007 (2012).

[10] J. Shi, S. Yazdi, S. C. S. Lin, X. Ding, I. K. Chiang, K. Sharp, and T. J. Huang, "Three-dimensional continuous particle focusing in a microfluidic channel via standing surface acoustic waves (SSAW)," *Lab on a Chip*, **11**, 2319-2324 (2011).

[11] P. B. Muller, R. Barnkob, M. J. H. Jensen, and H. Bruus, "A numerical study of microparticle acoustophoresis driven acoustic radiation forces and streaming-induced drag forces," *Lab on a Chip*, **12**, 4617-4627 (2012).

[12] N. A. Ramli, and A. N. Nordin, "Design and Modeling of MEMS SAW Resonator on Lithium Niobate," *2011 4th International Conference on Mechatronics (ICOM)*, Kuala Lumpur, Malaysia (2011).